European Journal of Medicinal Chemistry 276 (2024) 116715

Contents lists available at ScienceDirect

European Journal of Medicinal Chemistry

journal homepage: www.elsevier.com/locate/ejmech

Research paper

Novel tetrasubstituted 5-Arylamino pyrazoles able to interfere with angiogenesis and Ca^{2+} mobilization

Matteo Lusardi [a], Raffaella Belvedere [b], Antonello Petrella [b], Erika Iervasi [c], Marco Ponassi [c], Chiara Brullo [a], Andrea Spallarossa [a,*]

[a] Department of Pharmacy, Section of Medicinal Chemistry, University of Genoa, Viale Benedetto XV 3, I-16132, Genova, Italy
[b] Department of Pharmacy, University of Salerno, Viale Giovanni Paolo II, 84084, Salerno, Italy
[c] IRCCS Ospedale Policlinico San Martino, Proteomics and Mass Spectrometry Unit, Largo. R. Benzi, 10, 16132, Genova, Italy

ARTICLE INFO

Handling Editor: Dr. Z Liu

Keywords:
5-Arylaminopyrazoles
Angiogenesis
Cancer
Cell migration
Endothelial tube formation
Calcium homeostasis

ABSTRACT

In the last years, 5-pyrazolyl ureas and 5-aminopyrazoles have been investigated for their antiangiogenetic properties and their potential interaction with the ubiquitous Ca^{2+} binding protein Calreticulin. Based on the structure of the active compounds **I** and **GeGe-3**, novel 5-arylamino pyrazoles **2** and **3** were synthesized through a stepwise procedure. In MTT assays, all the new derivatives proved to be non-cytotoxic against eight different tumor cell lines, normal fibroblasts, and endothelial cells. Furthermore, selected derivatives showed relevant antiangiogenetic properties, resulting more effective than reference molecules **I** and **GeGe-3** in inhibiting HUVEC endothelial tube formation. 5-Arylamino pyrazoles **2a** and **2d** were identified as the most interesting compounds and significantly prevented tube formation of tumor secretome-stimulated HUVEC. Furthermore, the two compounds inhibited HUVEC migration in wound healing assay and altered cell invasion capability. Additionally, **2a** and **2d** strongly affected Ca^{2+} mobilization and cytoskeletal organization of HUVEC cells, being as active as the reference compound **GeGe-3**. Differently from previous studies, molecular docking simulations suggested a poor affinity of **2a** towards Calreticulin, one of the interacting partners of the lead compound **GeGe-3**. Collectively, this new amino-pyrazole library further extends the structure-activity relationships of the previously prepared derivatives and confirmed the biological attractiveness of this chemical scaffold as antiangiogenetic agents.

1. Introduction

Angiogenesis is the process in which new blood vessels are formed from a pre-existing vascular plexus. This process is involved in different physiological events including wound healing, fetal development, tissue growth and repair [1–4] and it is finely regulated by the balance between pro-angiogenic (e.g. vascular endothelial growth factor (VEGF) and angiopoietin) and anti-angiogenic factors (such as angiostatin and thrombospondin) [5]. The control mechanisms are induced through activation of several serine/threonine kinases in the mitogen-activated protein kinase (MAPK) (e.g. ERK1/2 and p38MAPK) and in the phosphatidylinositol 3-kinase (PI3K) (e.g. Akt and PKB) signaling pathways [6,7]. Moreover, calcium homeostasis strongly affects a wide variety of biological processes, including wound healing and angiogenesis [7,8]. In this context, the ubiquitous and highly conserved Ca^{2+} binding protein Calreticulin (CALR) has been recognized as a relevant factor in the regulation of PI3K and Akt signaling pathways, being involved in many biological activities such as cell adhesion, antigen presentation, apoptosis and anti-tumor immune response process [9–11].

In the last years, 5-pyrazolyl ureas have been largely investigated for their remarkable anti-inflammatory and antiangiogenetic properties [12–16]. In particular, compound **GeGe-3** (Fig. 1) potently interfered with p38MAPK and ERK pathways in VEGF-stimulated HUVEC. Furthermore, the derivative was able to inhibit HUVEC migration in wound healing assay and the intersegmental tube formation in zebrafish embryos, as well as the pathological angiogenesis of tumor in mice [13,17]. Additionally, in functional proteomics investigations on HUVEC, **GeGe-3** proved to affect intracellular Ca^{2+} levels in a dose dependent fashion through the interaction with CALR [18]. More recently, a novel series of 5-phenylamino pyrazole derivatives was synthesized and evaluated as antiangiogenetic agents on Human Foreskin Fibroblasts (HFF) and HUVEC [19]. Among the tested compounds, pyrazole **I** (Fig. 1) proved to be the most active, being able to inhibit Akt phosphorylation in HUVEC more efficiently than the reference compound

* Corresponding author.
E-mail address: andrea.spallarossa@unige.it (A. Spallarossa).

https://doi.org/10.1016/j.ejmech.2024.116715
Received 22 May 2024; Received in revised form 15 July 2024; Accepted 24 July 2024
Available online 30 July 2024

GeGe-3 and to interfere with HFF migration in wound healing assays. Moreover, docking simulation studies pointed out a possible interaction of compound **I** with CALR, thus highlighting a similar mechanism of action of **GeGe-3** [19]. To further improve the anti-angiogenic properties of **GeGe-3** and **I**, we designed and synthesized a novel series of 5-arylamino pyrazoles **2** and **3** (Fig. 1), bearing all the key structural determinant for the antiangiogenetic activity. In detail, the new molecules share with **I** and **GeGe-3** the N^1- hydroxypentyl or hydroxyphenyl chains as well as the primary amine and the carboxyethyl groups on the pyrazole core. Differently from their parent compounds, the novel derivatives presented variously substituted aryl-amino moieties at 3-position that mimic the urea or the phenylamino functionalities of the previously synthesized molecules. To define consistent SARs, electron withdrawing (i.e., Cl and CF_3) or electron donating (i.e., Me and OMe) groups were inserted at different positions on the phenyl amino moiety. Additionally, to evaluate the effects of steric hindrance on activity, 3, 4-dichlorophenyl and 1-naphthyl substructures were considered as Ar substituents (Fig. 1, Scheme 1).

2. Results and discussion

2.1. Chemistry

The novel 5-arylamino pyrazoles **2** and **3** were synthesized through the already reported stepwise procedure (Scheme 1) [19,20]. Briefly, the condensation of ethyl cyanoacetate with differently substituted aryl isothiocyanates in the presence of sodium hydride and the subsequent in situ S-methylation allowed the isolation of ketene *N,S*-acetals **1a-h**. The solvent free cyclization reaction with 2-hydrazineyl-1-phenylethan-1-ol (**Hy_1**; Scheme 1) or 1-hydrazineylpentan-2-ol (**Hy_2**; Scheme 1), prepared by condensing the proper epoxide with hydrazine monohydrate, confirmed to be highly chemo- and regioselective, leading to the unique formation of N-substituted pyrazoles **2a-h** and **3a-f** (Scheme 1). In fact, despite the possible isolation of two N-substituted pyrazoles, the condensation of intermediates **1** with sterically hindered hydrazines led to a single pyrazole isomer, bearing the substitution on the nitrogen atom adjacent to the free amino group [19–21].

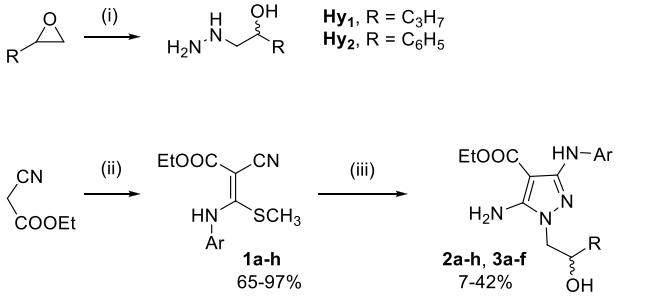

Cpd	Ar
1a	C_6H_5
1b	(2-Cl)C_6H_4
1c	(3-CF_3)C_6H_4
1d	(3-Cl)C_6H_4
1e	(4-CH_3)C_6H_4
1f	(4-OCH_3)C_6H_4
1g	(3,4-Cl_2)C_6H_3
1h	1-naphtyl

Cpd	Ar	R
2a	C_6H_5	C_3H_7
2b	(2-Cl)C_6H_4	C_3H_7
2c	(3-CF_3)C_6H_4	C_3H_7
2d	(3-Cl)C_6H_4	C_3H_7
2e	(4-CH_3)C_6H_4	C_3H_7
2f	(4-OCH_3)C_6H_4	C_3H_7
2g	(3,4-Cl_2)C_6H_3	C_3H_7
2h	1-naphtyl	C_3H_7
3a	(2-Cl)C_6H_4	C_6H_5
3b	(3-CF_3)C_6H_4	C_6H_5
3c	(3-Cl)C_6H_4	C_6H_5
3d	(4-OCH_3)C_6H_4	C_6H_5
3e	(3,4-Cl_2)C_6H_3	C_6H_5
3f	1-naphtyl	C_6H_5

Scheme 1. Synthesis of hydrazines **$Hy_{1,2}$** and pyrazoles **2** and **3**. Reagents and conditions: (i) $NH_2NH_2 \bullet H_2O$, 90–95 °C, 15 min; (ii) NaH (60 % dispersion in mineral oil), proper arylisothiocyanate, dry DMF; then iodomethane, rt, 16h; (iii) **Hy_1** or **Hy_2**, 80 °C, 2h.

2.2. Anti-proliferative activity

To verify the absence of cytotoxicity, compounds **2** and **3** were tested by MTT assay at a fixed concentration of 10 μM against a panel of tumor and normal cell lines. Cisplatin was used as reference drug at the concentration of 10 μM. In detail, MCF7, MDA-MB231, SK-Br3 (breast cancer cells), SKMEL-28 (melanoma cells), SKOV-3 (ovarian cancer cells), Hep-G2 (liver cancer cells), HeLa (cervical cancer cells), A549 (lung cancer cells), GM-6114 (normal human fibroblasts) and HUVEC were considered for the antiproliferative evaluation. As reported in Table 1, all tested derivatives did not show significant anti-proliferative activity against the considered cancer cell lines, displaying growth inhibition percentage values higher than 66 %. Additionally, the new molecules did not alter the viability of either normal fibroblasts GM-6114 (mean growth percentage range: 63–112 %) or HUVEC cells. The collected data indicated that neither the nature of the pyrazole side chain (i.e., 2-hydroxypentyl or 2-hydroxy-2-phenylethyl) nor the different electronic and steric properties of the aryl-amino moiety affected the antiproliferative profile of compounds **2** and **3**.

2.3. Endothelial cells tube formation

To preliminary evaluate the antiangiogenetic properties, derivatives **2** and **3** were tested at the fixed concentration of 10 μM for their inhibitory action on HUVEC tube formation, taking **GeGe-3** (10 μM) and **I** as references. HUVEC cells were seeded on the top of Matrigel and were incubated in presence of the compounds for 12 h without any stimulation. Untreated cells were used as control conditions and the number of tube branching points as well as the relative tube length were analyzed.

As reported in Fig. 2, compounds **2a,d-g** and **3c,f** significantly ($p \leq 0.05$) reduced tube length and branching, and pyrazoles **2a,e,h** and **3f** (branching points <15 and relative tube length <20; $p \leq 0.001$; Fig. 2) emerged to be more effective than the reference compounds **GeGe-3** (branching points = 19 and relative tube length = 21; $p \leq 0.001$; Fig. 2)

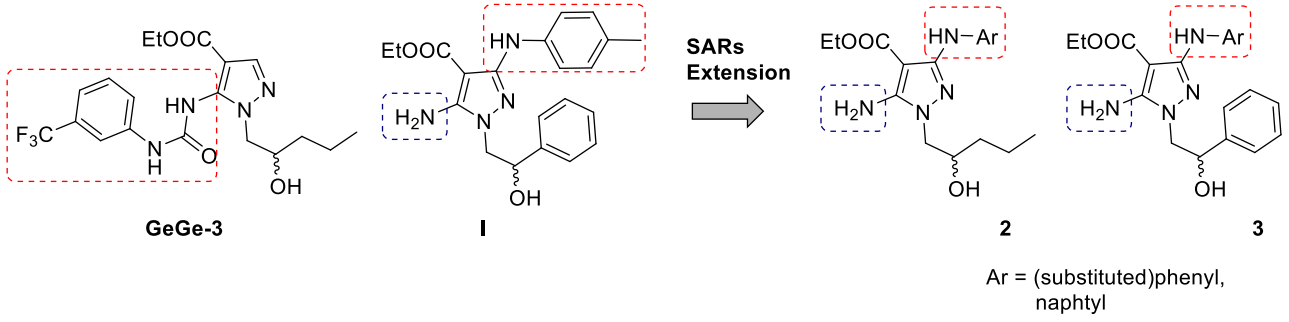

Fig. 1. General structures of previously synthesized derivatives **GeGe-3** and **I** and novel compounds **2** and **3**.

Table 1
Anti-proliferative activity of compounds **2**, **3** and Cisplatin used as reference compound.

Cpd	Growth percent (%)[a] ± SD									
	SKMEL-28	SKOV3	MCF7	A549	Sk-Br3	HeLa	Hep-G2	MDA-Mb231	GM-6114	HUVEC
2a	97 ± 7	104 ± 5	110 ± 5	115 ± 9	107 ± 3	97 ± 9	106 ± 2	103 ± 10	112 ± 13	100 ± 2
2b	132 ± 3	102 ± 3	110 ± 3	106 ± 9	121 ± 6	116 ± 5	119 ± 8	107 ± 2	85 ± 4	95 ± 6
2c	113 ± 5	102 ± 2	80 ± 4	66 ± 6	118 ± 4	77 ± 6	69 ± 6	109 ± 5	71 ± 2	100 ± 6
2d	122 ± 3	118 ± 2	95 ± 3	85 ± 7	113 ± 1	100 ± 2	90 ± 5	168 ± 9	82 ± 1	97 ± 4
2e	137 ± 5	119 ± 2	111 ± 9	92 ± 9	123 ± 5	109 ± 7	119 ± 9	158 ± 9	72 ± 1	96 ± 3
2f	120 ± 3	110 ± 2	109 ± 5	98 ± 4	106 ± 3	111 ± 9	110 ± 4	143 ± 2	75 ± 7	95 ± 5
2g	137 ± 10	116 ± 2	107 ± 4	94 ± 5	127 ± 5	119 ± 8	116 ± 9	176 ± 1	87 ± 5	93 ± 2
2h	103 ± 8	108 ± 4	109 ± 5	86 ± 8	110 ± 4	82 ± 9	104 ± 4	106 ± 11	104 ± 15	94 ± 3
3a	136 ± 3	100 ± 3	112 ± 4	72 ± 7	117 ± 3	98 ± 5	111 ± 6	115 ± 5	63 ± 5	93 ± 4
3b	124 ± 1	108 ± 2	99 ± 4	88 ± 1	122 ± 3	107 ± 3	131 ± 2	162 ± 9	80 ± 2	92 ± 2
3c	144 ± 5	100 ± 2	101 ± 2	88 ± 2	120 ± 3	113 ± 7	113 ± 6	135 ± 8	65 ± 5	93 ± 3
3d	134 ± 3	102 ± 3	98 ± 3	100 ± 9	115 ± 3	111 ± 8	115 ± 6	147 ± 8	70 ± 7	99 ± 5
3e	135 ± 5	111 ± 3	88 ± 3	70 ± 3	111 ± 5	74 ± 4	100 ± 6	144 ± 7	77 ± 1	93 ± 5
3f	141 ± 5	116 ± 4	97 ± 4	88 ± 5	118 ± 10	104 ± 7	118 ± 2	149 ± 9	81 ± 1	98 ± 4
CisPt	44 ± 3	37 ± 4	73 ± 5	59 ± 6	71 ± 4	29 ± 2	38 ± 2	86 ± 7	40 ± 3	ND

[a] Data mean values for three separate experiments; ND = not determined.

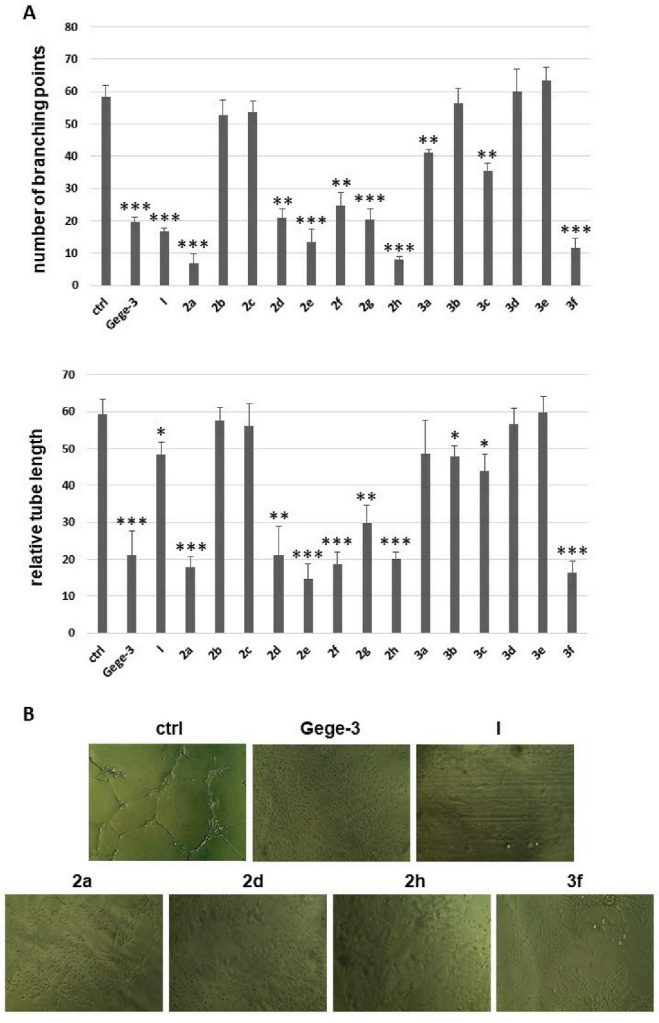

Fig. 2. A) Number of branching points and analysis of tube length calculated with ImageJ (Angiogenesis Analyzer tool); all the data represent a mean of at least three independent experiments. Significant differences from control conditions are indicated by asterisks (*p ≤ 0.05, **p ≤ 0.01, ***p ≤ 0.001); B) Representative images of tube formation of endothelial cells (HUVEC). 5-Arylamino pyrazoles and **GeGe-3** were tested at 10 μM concentration.

and **I** (branching points = 17 and relative tube length = 48; $p \leq 0.001$; Fig. 2). Both the chain on the pyrazole nitrogen and the substituents of the arylamino portion affected activity. Thus, the pentan-2-ol analogues **2** were more effective than their 1-phenyl-ethan-1-ol congeners **3**, exception made for the α-naphthyl derivative **3f** (Fig. 2). Additionally, among derivatives **2**, pyrazoles **2a** (Ar = phenyl), **2e** (Ar = (4-CH_3)C_6H_4) and **2h** (Ar = α-naphthyl) emerged to be highly effective. The decoration of phenylamino ring with 2-chloro (**2b**) or 3-trifluoromethyl (**2c**) groups strongly reduced compound's activity (comparing **2b** and **2c** with **2a** and **2e**), whereas the insertion of 3-chloro (**2d**), 4-methoxy (**2f**) and 3,4-dichloro (**2g**) moderately decreased anti-angiogenic properties. Overall, compounds **2** showed a widespread activity, indicating the biological attractiveness of this chemical scaffold for the development of novel angiogenesis inhibitor.

2.4. Wound healing assay and cell invasion capability

As eloquently demonstrated [22–24], new blood vessel formation is a critical component of wound healing and directly influence the cell invasion capability in the wound tissue. Additionally, the repair mechanism requires dynamic temporally and spatially regulated interactions between endothelial cells, angiogenesis factors and the proteins of extracellular matrix complex [23,24]. Considering the obtained result in the preliminary endothelial tube formation assay (Fig. 2), derivatives **2a** and **2d** were selected and tested by wound healing assay on HUVEC. After becoming confluent, HUVEC cells were gently injured with a sterile plastic tip to create a scratch which could heal by migration towards the scratched area. The wounds were imaged immediately afterwards the scratch formation and after 24 h of incubation. As reported in Fig. 3A, in the presence of derivatives **2a** and **2d** at 10 μM, cells strongly lost their ability to migrate towards the scratch areas after 24 h of treatment (distance = 548 μm and 546 μm, $p < 0.001$; Fig. 3B), in a very similar manner of the reference compound **GeGe-3** (distance = 446 μm, $p < 0.001$; Fig. 3B). To further explore the migration inhibition properties of the selected molecules, the cell invasion capability was evaluated on HUVEC (Fig. 3C). As observed in the wound healing assay, pyrazoles **2a** and **2d** exhibited a significant inhibition of cell invasion, being as active as the reference compound **GeGe-3**. In detail, compound **2a** displayed a lower number of cell (364, $p < 0.001$; Fig. 3D) in comparison with **GeGe-3** (383, $p < 0.001$; Fig. 3D), while derivative **2d** resulted to be less active (number of cells = 491, $p < 0.001$; Fig. 3D). Overall, the obtained results confirmed the influence of the compounds on cell migration and highlighted their potential role as anti-angiogenic agents.

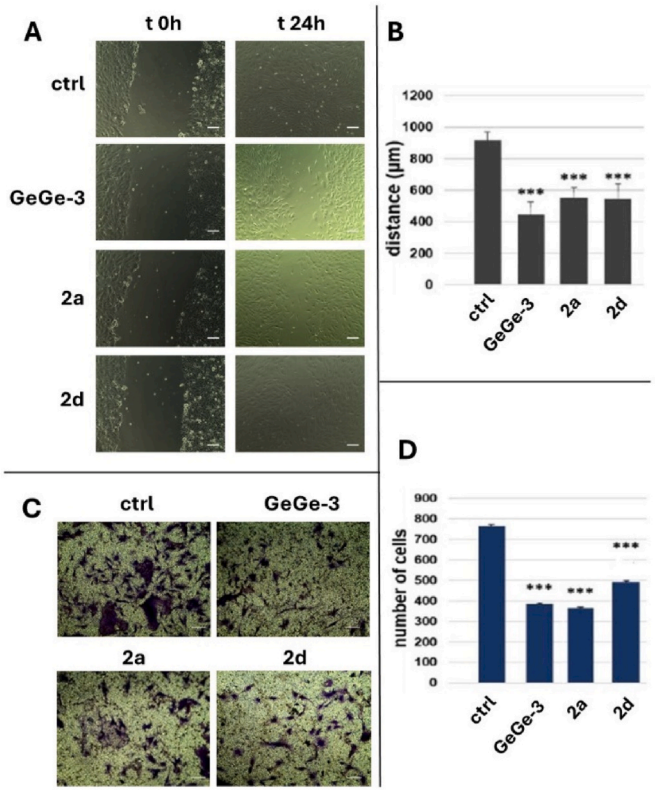

Fig. 3. A) Representative images of migration analysis of compounds **2a** and **2d** on wound healing assay in HUVEC. Scale bar = 100 μm; B) Results from the migration assay on HUVEC treated with **2a** and **2d** for 24h; C) Representative analysis of the invasion of HUVEC. Scale bar = 100 μm; D) Results of the HUVEC invasion at the same experimental point; the data represent the mean of n = 3 independent experiments ± SD; significant differences from control conditions are indicated by asterisks (*p ≤ 0.05, **p ≤ 0.01, ***p ≤ 0.001).

2.5. Effects of **2a** and **2d** on in vitro angiogenesis induced by pancreatic cancer (PC) tumor cells

During angiogenesis process, pro-angiogenic factors such as VEGF, bFGF, Platelet-Derived Growth Factor (PDGF), cytokines and small non-coding RNAs are initially secreted into the extracellular fluid. This complex mixture constitutes the so called secretome and promotes the formation of a new functional vascular network through the activation of endothelial cells [25,26]. In this scenario, the evaluation of the effect on tube formation in tumor secretome-stimulated HUVEC could represent a valid pathological model for angiogenesis. Thus, the most active derivatives **2a** and **2d** and reference **GeGe-3** were tested on HUVEC cells treated with the supernatant of MIA PaCa-2 pancreatic cancer cells (MIA PaCa-2 sup). Noteworthy, pancreatic cancer is considered a morphologically and functionally heterogeneous tumor that can be difficult to treat as its highly angiogenetic trend leads to remote metastasis and local recurrence, even after surgical treatment [27]. In detail, the supernatant was harvested from cells after 72 h of serum starvation (serum starved –SS– medium), to induce the release the majority of factors able to promote the main processes at the base of tumor progression, as well as the promotion of tube formation of the endothelial cells. HUVEC cells were then seeded on to the top of Matrigel coating and were incubated in presence of the compounds (10 μM concentration) for 12 h with MIA PaCa-2 sup in a 1:1 ratio with the HUVEC growth medium. Untreated cells were used as control (ctrl) and the number of tube branching points as well as the relative tube length were analyzed. As reported in Fig. 4, MIA PaCa-2 sup promote tube formation (branching points = 17 and relative tube length = 108) compared to ctrl cells (branching points = 9; relative tube length = 65; $p \leq 0.05$). Additionally, compounds **2a** and **2d** markedly inhibit the angiogenic effect induced by MIA PaCa-2 sup, by reducing both tube length and branching points (branching points ≈8 and relative tube length in the 55–65 range; $p \leq 0.01$; Fig. 4). Interestingly, the activity of tested derivatives emerged to be similar to that of **GeGe-3** compound.

Noteworthy, the activity of compounds **2a** and **2d** on secretome-induced angiogenesis is consistent with that observed on unstimulated HUVEC cells (Fig. 2) and parallel the inhibitory effect of **GeGe-3** on the formation of capillary-like structures in HUVEC treated with MIA PaCa-2-derived exosomes [16].

2.6. Effects of **2a** and **2d** on calcium mobilization and F-actin organization

Based on the previous evidence which indicated a possible

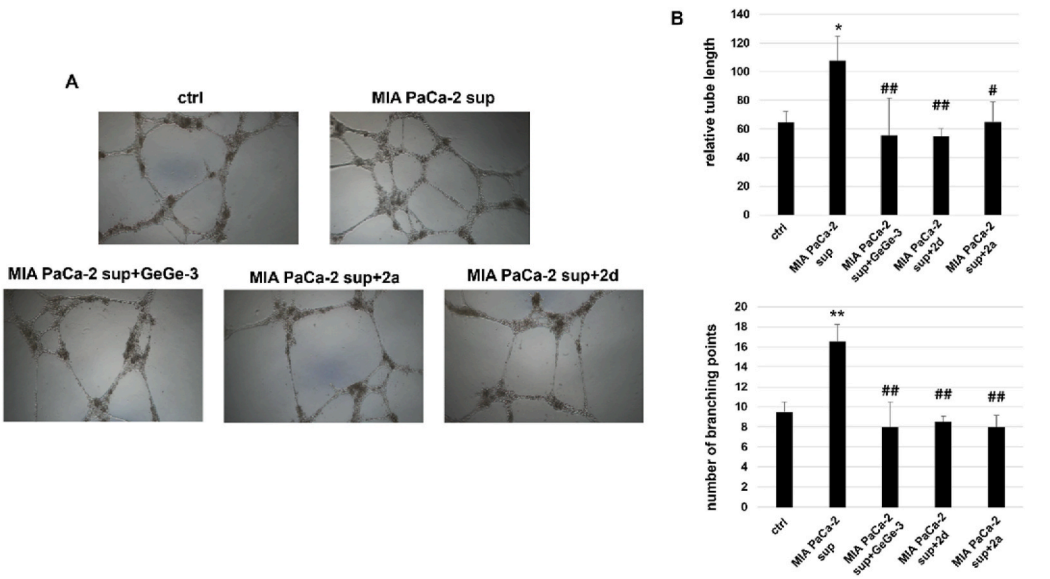

Fig. 4. A) Representative images of tube formation of HUVEC in response to MIA PaCa-2 SS supernatant (sup) with and without **2a**, **2d** and **GeGe-3** (10 μM). B) Number of branching points and tube length analyses; all the data represent a mean of three independent experiments. Significant differences from control conditions are indicated by asterisks vs ctrl (*p ≤ 0.05; **p ≤ 0.01) and by hashtag vs MIA PaCa-2 sup (#p ≤ 0.05; ##p ≤ 0.01).

interaction between **GeGe-3** and **I** with CALR [18,19], the regulation of Ca^{2+} homeostasis in HUVEC cells have been investigated. Indeed, CALR is directly involved in the regulation of intracellular Ca^{2+} homeostasis and endoplasmic reticulum Ca^{2+} capacity, influencing the folding and the quality control of the newly synthesized proteins and glycoproteins [28]. As reported in Fig. 5A, the Fluo-4 a.m. cytofluorimetric assay showed that 5-arylamino **2a** and **2d** inhibited the calcium mobilization with similar fluorescence intensity percentage values of the reference compound **GeGe-3** (23 and 21 versus 20, $p < 0.001$ %; Fig. 5A). Ionomycin and EDTA were used as positive and negative control, respectively. Additionally, since Ca^{2+} mobilization represents a crucial step for the cytoskeletal assembling [29], the organization of F-actin of HUVEC cells in the presence of derivatives **2a** and **2d** was investigated (Fig. 5B).

The immunofluorescence assay on cytoskeleton was carried out using the compounds and the reference compound **GeGe-3** at 10 μM concentration. Interestingly, the well-structured actin filaments organized in stress fibers in not treated cells markedly lost their conformation in the presence of pyrazoles **2a** and **2d**, as well as the treatment with **GeGe-3** (Fig. 5B). The inhibition of Ca^{2+} mobilization and the influence on cytoskeletal organization further support the hypothesis of a potential interaction of the new synthesized derivatives with Ca^{2+} homeostasis and confirmed their biological attractiveness.

2.7. Docking studies

The structural similarity between pyrazoles **GeGe-3** and **2a** as well as their homologous behavior in the antiangiogenetic and calcium mobilization assays, prompted us to carried out docking simulation (Autodock 4.2) to evaluate the binding potential of **2a** towards CALR, one of the interacting partners of lead compound **GeGe-3** [18]. Thus, in CALR/(R)-**2a** and CALR/(S)-**2a** docking complexes the ligand would assume similar orientation with the pyrazole 2-hydroxypentyl chain and the phenylamino portion inserted in the binding pocket whereas the ammino and ester groups would point towards the solvent (Fig. 6A).

Despite the docking poses of **2a** enantiomers would be different from those previously calculated for **GeGe-3** [18], the 2-hydroxypentyl chain of the two ligands would be similarly oriented within the binding site and equally involved in complex stabilization. In particular, the alcoholic group of **GeGe-3** and **2a** 2-hydroxypentyl chain would be able to form H-bonds with Tyr109 and Asp317 side chains (Fig. 6B and C). The CALR/(R)-**2a** and CALR/(S)-**2a** complexes would be further stabilized by and additional H-bond between the phenylamino NH group and Asp125 side chain. Additional stabilization to the complexes would be provided by van der Waals interactions between **2a** phenyl ring and Phe46, Phe74, His123 and Gly124 residues; furthermore, **2a** pyrazole nucleus would interact with Gly124 and Asp125 and 2-hydroxypentyl carbon chain would be in contact with Phe74, Tyr109, Asp317 and Trp319 side chains. Unexpectedly, the calculated Ki values for CALR/(R)-**2a** and CALR/(S)-**2a** complexes were 5.05 mM and 5.10 mM, respectively, thus resulting one order of magnitude higher than those predicted for **GeGe-3** enantiomers (i.e., Ki(R) = 503 μM and Ki(S) = 510 μM).

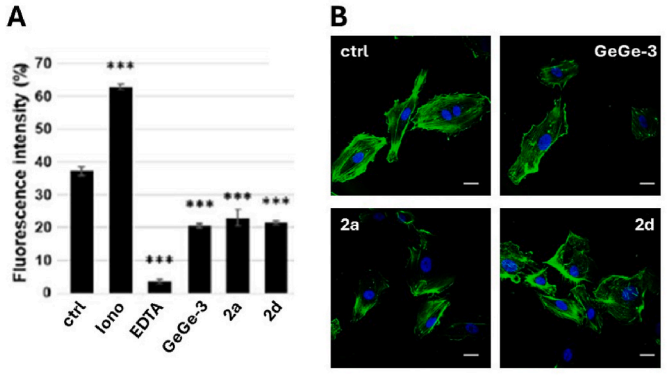

Fig. 5. A) Effects of ionomycin (1 mM), EDTA (15 mM), **GeGe-3**, **2a** and **2d** (10 μM) on rise in intracellular Ca^{2+} in HUVEC cells. The histogram shows the fluorescence increment related to the amount of calcium intracellular; the data represent the mean of n = 3 independent experiments ± SD; significant differences from control conditions are indicated by asterisks (*$p \leq 0.05$, **$p \leq 0.01$, ***$p \leq 0.001$); B) Confocal analysis for F-actin of HUVEC cells untreated or treated for 24 h with 10 μM **GeGe-3**, **2a** and **2d**. Magnification 63 × 1.4NA. Bar = 10 μm.

3. Conclusion

Based on the molecular structure of the antiangiogenetic pyrazolyl derivatives **GeGe-3** and **I**, compounds **2** and **3** were designed and synthesized. The novel derivatives bear all the structural determinants for the antiangiogenetic activity: a free amino group and a carboxyethyl functionality on the pyrazole core, a hydroxypentyl or hydroxy phenyl chain at N^1 pyrazole and differently decorated aryl substituents at 3-position. All the new isolated molecules were screened at the final concentration of 10 μM by MTT assay against a panel of eight tumor cell lines, normal fibroblasts and HUVECs proving to be non-cytotoxic. The antiangiogenetic properties of the series were evaluated in HUVECs by endothelial tube formation assay. Selected derivatives exhibited a good inhibition of tube formation, being more active than the reference compounds **I** and **GeGe-3**. Particularly, 5-arylamino pyrazoles **2a** and **2d** emerged as the most promising derivatives and proved to significant inhibit repair of scratched areas in wound healing assay and to block the HUVEC cell invasion capability. Interestingly, the two compounds showed significative activity in a MIA PaCa-2 secretome-induced angiogenesis, considered as a pathological model for new vessel formation. Additionally, **2a** and **2d** seemed to interfere with Calcium mobilization in HUVEC cells and to alter the F-actin organization in cytoskeleton in the same way of the reference compound **GeGe-3**. Docking simulations carried out on derivative **2a** indicated a poor propensity of the compound to bind CALR, being the calculated Ki values in the millimolar concentration range. Overall, the obtained results confirmed the biological potential of derivatives **2** and **3** as novel antiangiogenetic agents and highlighted their role on calcium homeostasis and cytoskeletal organization. Despite the structural and functional similarities among the compounds, docking simulations would not support an effective interaction between **2a** and CALR, one of the interacting partners of **GeGe-3**. To elucidate the mechanism of action behind their relevant antiangiogenetic properties, future proteomic investigations will be carried out to identify the interactome of derivatives **2** and **3**.

4. Materials and methods

4.1. Chemistry

Ethyl cyanoacetate, aryl isothiocyanates, hydrazine monohydrate, and reagents (60 % sodium hydride dispersion in mineral oil and iodomethane) were purchased by Alfa-Aesar and Sigma-Aldrich. DMF was reagent grade and was dried on molecular sieves (5 Å 1/16″ inch pellets). Unless otherwise stated, all commercial reagents were used without further purification. Organic solutions were dried over anhydrous sodium sulphate. A thin layer chromatography (TLC) system for routine monitoring the course of reactions and confirming the purity of analytical samples employed aluminum-backed silica gel plates (Merck DC-Alufolien Kieselgel 60 F254). Neat DCM or DCM/2 % methanol mixture were used as a developing solvent and detection of spots was made by UV light and/or by iodine vapors. Melting points were determined on a Fisher-Johns apparatus and are uncorrected. ^{1}H NMR and ^{13}C NMR spectra were recorded on a Varian Gemini (200 MHz Palo Alto, California, USA) or JEOL JNMECZR (400 MHz, Tokyo, Japan); chemical shifts were reported in δ (ppm) units relative to the internal reference

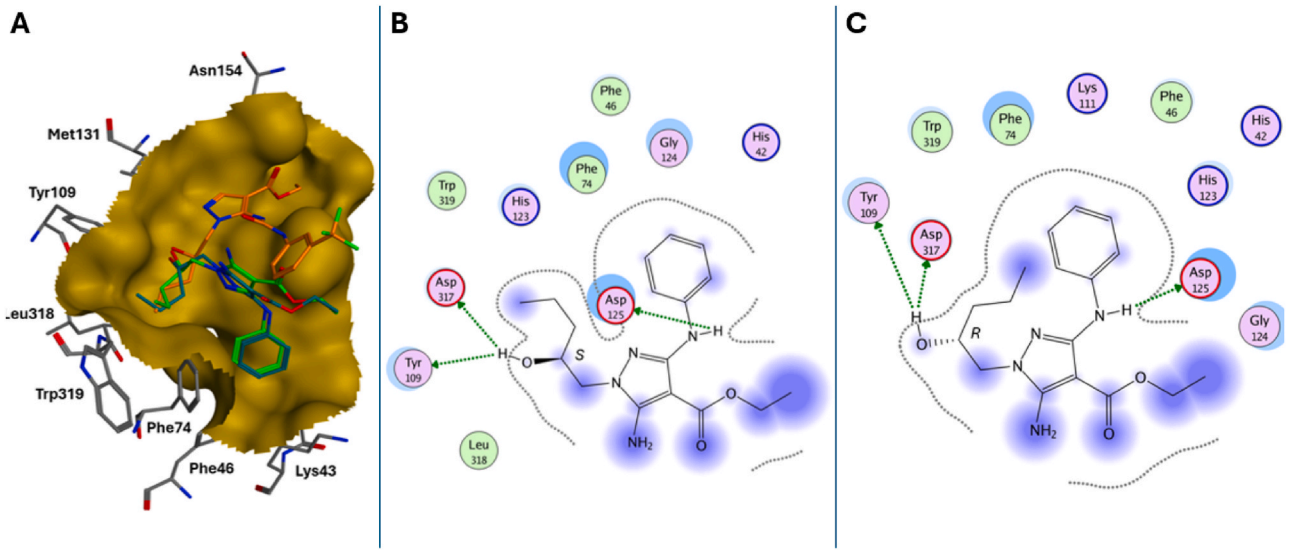

Fig. 6. A) Superposition of the docking poses calculated for (R)**GeGe3** (orange), (S)-**2a** (green) and (R)-**2a** (dark green) within CALR binding site. B) Ligplot of CALR/(S)-**2a** docking complex. C) Ligplot of CALR/(R)-**2a** docking complex.

tetramethylsilane, and the splitting patterns were described as follows: s (singlet), bs (broad singlet), d (doublet), t (triplet), q (quartet), and m (multiplet). The first order values reported for coupling constants J were given in Hz. Elemental analyses were determined by an EA1110 Analyzer, Fison Instruments (Milan, Italy). Compounds $\mathbf{Hy_1}$ and $\mathbf{Hy_2}$ were prepared as previously reported [17,19].

*4.1.1. General synthetic procedure for the preparation of intermediates **1***

To a dry DMF solution (10 mL) of ethyl cyanoacetate (1085 μL, 10 mmol), 60 % sodium hydride dispersion in mineral oil (0.44 g, 10 mmol) and the proper aryl isothiocyanate (10 mmol) were sequentially added under stirring at 0 °C. The mixture was stirred at rt for 2 h and then methyl iodide (629 μL, 10 mmol) was added prolonging stirring at rt for 16 h. The reaction mixture was cooled, treated with water (50 mL) and the precipitated solid was collected by filtration, dried and used without further purification.

4.1.1.1. Ethyl 2-cyano-3-(methylthio)-3-(phenylamino)acrylate 1a. Yield: 65 %. Yellow solid. Mp 83–85 °C (water) (litt [30].: 82 °C). ^{1}H NMR (200 MHz, $CDCl_3$) δ 1.34 (t, J = 7.2 Hz, 3H, CH_3 ester), 2.23 (s, 3H, SCH_3), 4.27 (q, J = 7.2 Hz, 2H, CH_2O), 7.21–7.49 (m, 5H, arom. H), 11.51 (bs, 1H, NH, exchangeable). Anal calcd for $C_{13}H_{14}N_2O_2S$: C: 59.52; H: 5.38; N: 10.68; S: 12.22. Found: C: 59.82; H: 5.42; N: 10.60; S: 11.37.

4.1.1.2. Ethyl 3-((2-chlorophenyl)amino)-2-cyano-3-(methylthio)acrylate 1b. Yield: 81 %. Yellow solid. Mp 130–132 °C (water). ^{1}H NMR (400 MHz, $CDCl_3$) δ 1.36 (t, J = 7.2 Hz, 3H, CH_3 ester), 2.25 (s, 3H, SCH_3), 4.29 (q, J = 7.2 Hz, 2H, CH_2O), 7.25–7.35 (m, 2H, arom. H), 7.44–7.51 (m, 2H, arom. H), 11.36 (bs, 1H, NH, exchangeable). Anal calcd for $C_{13}H_{13}ClN_2O_2S$: C: 52.61; H: 4.42; N: 9.44; S: 10.80. Found: C: 52.89; H: 4.60; N: 9.13; S: 10.58.

4.1.1.3. Ethyl 2-cyano-3-(methylthio)-3-((3-(trifluoromethyl)phenyl) amino)acrylate 1c. Yield: 75 %. Yellow solid. Mp 111–114 °C (Water). ^{1}H NMR (400 MHz, $CDCl_3$) δ 1.35 (t, J = 7.1 Hz, 3H, CH_3 ester), 2.31 (s, 3H, SCH_3), 4.29 (q, J = 7.1 Hz, 2H, CH_2), 7.48–7.61 (m, 4H, arom. H), 11.58 (bs, 1H, NH, exchangeable). Anal calcd for $C_{14}H_{13}F_3N_2O_2S$: C: 50.91; H: 3.97; N: 8.48; S: 9.71. Found: C: 50.96; H: 4.16; N: 8.20; S: 9.63.

4.1.1.4. Ethyl 3-((3-chlorophenyl)amino)-2-cyano-3-(methylthio)acrylate 1d. Yield: 71 %. Brown solid. Mp 115–118 °C (water). ^{1}H NMR (400 MHz, $CDCl_3$) δ 1.35 (t, J = 7.1 Hz, 3H, CH_3 ester), 2.29 (s, 3H, SCH_3), 4.27 (q, J = 7.1 Hz, 2H, CH_2O), 7.18–7.22 (m, 1H, arom. H), 7.27–7.36 (m, 3H, arom. H), 11.47 (bs, 1H, NH, exchangeable). Anal calcd for $C_{13}H_{13}ClN_2O_2S$: C: 52.61; H: 4.42; N: 9.44; S: 10.80. Found: C: 52.39; H: 4.38; N: 9.36; S: 10.65.

4.1.1.5. Ethyl 2-cyano-3-(methylthio)-3-(p-tolylamino)acrylate 1e. Yield: 87 %. Brown solid. Mp 75–77 °C (water) (litt [31].: 79–81 °C). ^{1}H NMR (400 MHz, $CDCl_3$) δ 1.44 (t, J = 7.1 Hz, 3H, CH_3 ester), 2.35 (s, 3H, SCH_3), 2.46 (s, 3H, CH_3Ph), 4.36 (q, J = 7.1 Hz, 2H, CH_2O), 7.22–7.31 (m, 4H, arom. H), 11.55 (bs, 1H, NH, exchangeable). Anal calcd for $C_{14}H_{16}N_2O_2S$: C: 60.85; H: 5.84; N: 10.14; S: 11.60. Found: C: 60.79; H: 5.71; N: 9.95; S: 11.44.

4.1.1.6. Ethyl 2-cyano-3-((4-methoxyphenyl)amino)-3-(methylthio)acrylate 1f. Yield: 63 %. Yellow solid. Mp 89–91 °C (Water). ^{1}H NMR (400 MHz, $CDCl_3$) δ 1.35 (t, J = 7.1 Hz, 3H, CH_3 ester), 2.27 (s, 3H, SCH_3), 3.83 (s, 3H, OCH_3), 4.26 (q, J = 7.1 Hz, 2H, CH_2), 6.87–6.95 (m, 2H, arom. H), 7.14–7.22 (m, 2H, arom. H), 11.42 (bs, 1H, NH, exchangeable). Anal calcd for $C_{14}H_{16}N_2O_3S$: C: 57.52; H: 5.52; N: 9.58; S: 10.97. Found: C: 57.26; H: 5.63; N: 9.38; S: 10.94.

4.1.1.7. Ethyl 2-cyano-3-((3,4-dichlorophenyl)amino)-3-(methylthio) acrylate 1g. Yield: 97 %. White solid. Mp 124–126 °C (Water). ^{1}H NMR (400 MHz, $CDCl_3$) δ 1.35 (t, J = 7.1 Hz, 3H, CH_3 ester), 2.33 (s, 3H, SCH3), 4.27 (q, J = 7.1 Hz, 2H, CH_2), 7.14–7.19 (m, 1H, arom. H), 7.41–7.44 (m, 1H, arom. H), 7.45–7.50 (m, 1H, arom. H), 11.45 (bs, 1H, NH, exchangeable). Anal calcd for $C_{13}H_{12}Cl_2N_2O_2S$: C: 47.14; H: 3.65; N: 8.46; S: 9.68. Found: C: 47.08; H: 3.87; N: 8.07; S: 9.47.

4.1.1.8. Ethyl 2-cyano-3-(methylthio)-3-(naphthalen-1-ylamino)acrylate 1h. Yield: 88 %. White solid. Mp 115–117 °C (Water). ^{1}H NMR (400 MHz, $CDCl_3$) δ 1.39 (t, J = 7.1 Hz, 3H, CH_3 ester), 2.17 (s, 3H, SCH3), 4.32 (q, J = 7.1 Hz, 2H, CH_2), 7.41–7.64 (m, 4H, arom. H), 7.82–7.97 (m, 3H, arom. H), 11.80 (bs, 1H, NH, exchangeable). Anal calcd for $C_{17}H_{16}N_2O_2S$: C: 65.36; H: 5.16; N: 8.97; S: 10.26. Found: C: 65.15; H: 5.02; N: 8.87; S: 10.10.

*4.1.2. General procedure for the synthesis of pyrazoles **2** and **3***

A mixture of the proper intermediate **1** (3 mmol) and $\mathbf{Hy_1}$ (363 mg, 3

mmol) or **Hy$_2$** (466 mg, 3 mmol) was heated in a sealed tube at 80 °C for 2–4 h. The reaction mixture was cooled at rt and dissolved in DCM (10 mL). Evaporating in vacuo gave a crude residue which was purified by crystallization from the suitable solvent or solvent mixture or by column chromatography (silica gel, eluent: DCM-DCM/2 % MeOH).

4.1.2.1. Ethyl 5-amino-1-(2-hydroxypentyl)-3-(phenylamino)-1H-pyrazole-4-carboxylate 2a. Yield: 26 %. White solid. Mp 117–119 °C (Et_2O/Cyclohexane). ^{1}H NMR (400 MHz, DMSO-d_6) δ 0.81–0.93 (m, 3H, CH_3), 1.22–1.54 (m, 7H, CH_3 ester + 2xCH_2), 3.75–3.80 (m, 2H, NCH_2), 3.82–3.90 (m, 1H, CHOH), 4.24 (q, J = 7.0 Hz, 2H, CH_2O), 4.72 (bs, 1H, OH, exchangeable), 6.12 (bs, 2H, NH_2, exchangeable), 6.75–6.88 (m, 1H, arom. H), 7.15–7.31 (m, 2H, arom. H), 7.44–7.56 (m, 2H, arom. H), 8.05 (bs, 1H, NHPh, exchangeable). ^{13}C NMR (101 MHz, DMSO-d_6) δ 164.02, 149.83, 149.12, 141.42, 128.79, 119.55, 116.21, 81.95, 68.70, 58.91, 52.41, 36.35, 18.25, 14.57, 14.08. Anal calcd for $C_{17}H_{24}N_4O_3$: C: 61.43; H: 7.28; N: 16.86. Found: C: 61.28; H: 7.16; N: 16.98.

4.1.2.2. Ethyl 5-amino-3-((2-chlorophenyl)amino)-1-(2-hydroxypentyl)-1H-pyrazole-4-carboxylate 2b. Yield: 24 %. Yellow solid. Mp 143–145 °C (Ligroin/EtOH). ^{1}H NMR (400 MHz, DMSO-d_6) δ 0.83–0.91 (m, 3H, CH_3), 1.28–1.52 (m, 7H, CH_3 ester + 2xCH_2), 3.78–3.83 (m, 2H, NCH_2), 3.83–3.91 (m, 1H, CHOH), 4.27 (q, J = 7.1 Hz; 2H, CH_2O), 4.93–4.99 (m, 1H, OH, exchangeable), 6.20 (bs, 2H, NH_2, exchangeable), 7.23–7.32 (m, 1H, arom. H), 7.38–7.45 (m, 1H, arom. H), 7.57–7.64 (m, 1H, arom. H), 8.39–8.46 (m, 1H, arom. H), 8.72 (bs, 1H, NHPh, exchangeable). ^{13}C NMR (101 MHz, DMSO-d_6) δ 138.08, 130.42, 129.36, 128.58, 128.47, 120.73, 119.34, 117.48, 82.81, 69.13, 59.62, 53.02, 36.85, 18.75, 15.15, 14.58. Anal calcd for $C_{18}H_{26}N_4O_3$: C: 62.41; H: 7.57; N: 16.17. Found: C: 55.44; H: 6.00; N: 15.35.

4.1.2.3. Ethyl 5-amino-1-(2-hydroxypentyl)-3-((3-(trifluoromethyl)phenyl)amino)-1H-pyrazole-4-carboxylate 2c. Yield: 12 %. White solid. Mp 147–150 °C (Et_2O/Cyclohexane). ^{1}H NMR (400 MHz, DMSO-d_6) δ 0.80–0.91 (m, 3H, CH_3), 1.24–1.48 (m, 7H, CH_3 ester + 2xCH_2), 3.56–3.73 (m, 3H, NCH_2 + CHOH), 4.02–4.14 (m, 2H, CH_2O), 4.76–4.84 (m, 1H, OH, exchangeable), 6.02 (bs, 2H, NH_2, exchangeable), 6.91–6.99 (m, 1H, arom. H), 7.20–7.30 (m, 1H, arom. H), 7.45–7.55 (m, 1H, arom. H), 7.93–8.00 (m, 1H, arom. H), 8.14 (bs, 1H, NHPh, exchangeable). ^{13}C NMR (101 MHz, DMSO-d_6) δ 163.88, 149.30, 142.17, 129.66, 129.45, 125.81, 123.10, 120.09, 115.64, 112.28, 82.26, 68.59, 58.99, 52.33, 36.34, 18.24, 14.59, 13.95. Anal calcd for $C_{18}H_{23}F_3N_4O_3$: C: 54.00; H: 5.79; N: 13.99. Found: C: 53.93; H: 5.86; N: 13.74.

4.1.2.4. Ethyl 5-amino-3-((3-chlorophenyl)amino)-1-(2-hydroxypentyl)-1H-pyrazole-4-carboxylate 2d. Yield: 15 %. Yellow solid. Mp 129–132 °C (Et_2O/Cyclohexane). ^{1}H NMR (400 MHz, DMSO-d_6) δ 0.87 (t, J = 6.7 Hz, 3H, CH_3), 1.30 (t, J = 7.1 Hz, 3H, CH_3 ester), 1.33–1.53 (m, 4H, 2 x CH_2), 3.74–3.91 (m, 3H, NCH_2 + CHOH), 4.25 (q, J = 7.1 Hz, 2H, CH_2O), 4.93–5.00 (m, 1H, OH, exchangeable), 6.16 (bs, 2H, NH_2, exchangeable), 6.80–6.88 (m, 1H, arom. H), 7.18–7.27 (m, 1H, arom. H), 7.32–7.40 (m, 1H, arom. H), 7.80–7.85 (m, 1H, arom. H), 8.18 (bs, 1H, NHPh, exchangeable). ^{13}C NMR (101 MHz, DMSO-d_6) δ 163.88, 149.26, 142.86, 133.29, 130.22, 119.06, 115.58, 115.03, 82.19, 68.62, 58.97, 52.35, 36.33, 18.23, 14.57, 14.07. Anal calcd for $C_{17}H_{23}ClN_4O_3$: C: 55.66; H: 6.32; N: 15.27. Found: C: 55.68; H: 6.25; N: 15.34.

4.1.2.5. Ethyl 5-amino-1-(2-hydroxypentyl)-3-(p-tolylamino)-1H-pyrazole-4-carboxylate 2e. Yield: 24 %. Yellow solid. Mp 90–92 °C (Et_2O/Cyclohexane). ^{1}H NMR (400 MHz, DMSO-d_6) δ 0.79–0.92 (m, 3H, CH_3), 1.26–1.51 (m, 7H, CH_3 ester + 2xCH_2), 2.21 (s, 3H, CH_3Ph), 3.73–3.79 (m, 2H, NCH_2), 3.82–3.87 (m, 1H, CHOH), 4.24 (q, J = 7.1 Hz, 2H, CH_2O), 4.92–4.98 (m, 1H, OH, exchangeable), 6.10 (bs, 2H, NH_2, exchangeable), 6.99–7.06 (m, 2H, arom. H), 7.37–7.45 (m, 2H, arom. H), 7.94 (bs, 1H, NHPh, exchangeable). ^{13}C NMR (101 MHz, DMSO-d_6) δ 164.05, 150, 149.11, 139.05, 129.20, 128.12, 116.24, 81.82, 68.71, 58.87, 52.37, 36.35, 20.32, 18.26, 14.59, 14.09. Anal calcd for $C_{18}H_{26}N_4O_3$: C: 62.41; H: 7.57; N: 16.17. Found: C: 62.26; H: 7.40; N:16.31.

4.1.2.6. Ethyl 5-amino-1-(2-hydroxypentyl)-3-((4-methoxyphenyl)amino)-1H-pyrazole-4-carboxylate 2f. Yield: 6 %. Yellow solid. Mp 80–83 °C (Et_2O/Cyclohexane). ^{1}H NMR (400 MHz, DMSO-d_6) δ 0.87 (t, J = 6.8 Hz, 3H, CH_3), 1.26–1.51 (m, 7H, CH_3 ester + 2xCH_2), 3.69 (s, 3H, OCH_3), 3.72–3.79 (m, 2H, NCH_2), 3.80–3.89 (m, 1H, CHOH), 4.23 (q, J = 7.1 Hz, 2H, CH_2O), 4.92–4.99 (m, 1H, OH, exchangebale), 6.09 (bs, 2H, NH_2, exchangebale), 6.78–6.87 (m, 2H, arom. H), 7.41–7.50 (m, 2H, arom. H), 7.84 (bs, 1H, NHPh, exchangebale). ^{13}C NMR (101 MHz, DMSO-d_6) δ 164.03, 152.83, 150.19, 149.11, 135.13, 117.46, 114.07, 81.67, 68.70, 58.81, 55.19, 52.37, 36.36, 18.25, 14.59, 14.09. Anal calcd for $C_{18}H_{26}N_4O_4$: C: 59.65; H: 7.23; N: 15.46. Found: C: 59.45; H: 7.04; N: 15.21.

4.1.2.7. Ethyl 5-amino-3-((3,4-dichlorophenyl)amino)-1-(2-hydroxypentyl)-1H-pyrazole-4-carboxylate 2g. Yield: 13 %. White solid. Mp 117–120 °C (Et_2O/Cyclohexane). ^{1}H NMR (400 MHz, DMSO-d_6) δ 0.83–0.91 (m, 3H, CH_3), 1.26–1.50 (m, 7H, CH_3 ester + 2xCH_2), 3.74–3.90 (m, 3H, NCH_2 + CHOH), 4.20–4.29 (m, 2H, CH_2O), 4.94–5.00 (m, 1H, OH, exchangeable), 6.18 (bs, 2H, NH_2, exchangeable), 7.40–7.50 (m, 2H, arom. H), 8.00–8.05 (m, 1H, arom. H), 8.24 (bs, 1H, NHPh, exchangeable). ^{13}C NMR (101 MHz, DMSO-d_6) δ 163.78, 149.33, 148.99, 141.55, 130.93, 130.31, 120.44, 117.36, 116.82, 82.28, 68.58, 58.99, 52.37, 36.33, 18.23, 14.57, 14.07. Anal calcd for $C_{17}H_{22}Cl_2N_4O_3$: C: 50.88; H: 5.53; N: 13.96. Found: C: 51.02; H: 5.34; N: 14.04.

*4.1.2.8. Ethyl 5-amino-1-(2-hydroxypentyl)-3-(naphthalen-1-ylamino)-1H-pyrazole-4-carboxylate **2h**.* Yield: 18 %. White solid. Mp 127–130 °C (EtOH). ^{1}H NMR (400 MHz, DMSO-d_6) δ 0.84–0.93 (m, 3H, CH_3), 1.29–1.46 (m, 7H, CH_3 ester + 2xCH_2), 3.81–3.87 (m, 2H, NCH_2), 3.88–3.93 (m, 1H, CHOH), 4.33 (q, J = 7.1 Hz, 2H, CH_2O), 4.99 (bs, 1H, OH, exchangeable), 6.20 (bs, 2H, NH_2, exchangeable), 7.38–7.49 (m, 2H, arom. H), 7.50–7.67 (m, 2H, arom. H), 7.87–7.99 (m, 2H, arom. H), 8.25–8.36 (m, 1H, arom. H), 9.14 (bs, 1H, NHPh, exchangeable). ^{13}C NMR (101 MHz, DMSO-d_6) δ 164.67, 150.07, 149.05, 136.06, 133.74, 128.80, 126.49, 125.88, 125.79, 122.88, 119.47, 119.37, 110.79, 82.34, 68.71, 59.23, 52.57, 36.38, 18.27, 14.65, 14.10. Anal calcd for $C_{21}H_{26}N_4O_3$: C: 65.95; H: 6.85; N: 14.65. Found: C: 65.88; H: 6.70; N: 14.75.

*4.1.2.9. Ethyl 5-amino-3-((2-chlorophenyl)amino)-1-(2-hydroxy-2-phenylethyl)-1H-pyrazole-4-carboxylate **3a**.* Yield: 14 %. White solid. Mp 126–128 °C (Ligroin/EtOH). ^{1}H NMR (400 MHz, DMSO-d_6) δ 1.31 (t, J = 7.1 Hz, 3H, CH_3), 3.90–3.99 (m, 2H, NCH_2), 4.03–4.14 (m, 1H, CHOH), 4.27 (q, J = 7.1 Hz, 2H, CH_2O), 4.97–5.06 (m, 1H, CHPh), 5.64–5.69 (m, 1H, OH, exchangeable), 6.22 (bs, 2H, NH_2, exchangeable), 6.81–6.90 (m, 1H, arom. H), 7.22–7.46 (m, 7H, arom. H), 8.34–8.42 (m, 1H, arom. H), 8.65 (bs, 1H, NHPh, exchangeable). ^{13}C NMR (101 MHz, DMSO-d_6) δ 163.88, 142.67, 137.55, 128.78, 128.28, 128.07, 128, 127.45, 127.35, 126.35, 120.21, 118.82, 117.16, 82.26, 71.03, 59.08, 53.60, 14.62. Anal calcd for $C_{20}H_{21}ClN_4O_3$: C: 59.93; H: 5.28; N: 13.98. Found: C: 59.89; H: 5.29; N: 14.17.

4.1.2.10. Ethyl 5-amino-1-(2-hydroxy-2-phenylethyl)-3-((3-(trifluoromethyl)phenyl)amino)-1H-pyrazole-4-carboxylate 3b. Yield: 25 %. Yellow solid. Mp 128–131 °C (DCM/MeOH). ^{1}H NMR (400 MHz, DMSO-d_6) δ 1.30 (t, J = 7.1 Hz, 3H, CH_3), 3.88–3.97 (m, 2H, NCH_2), 4.04–4.14 (m, 1H, CHOH), 4.25 (q, J = 7.1 Hz, 2H, CH_2O), 4.99–5.08 (m, 1H, CHPh), 5.65–5.71 (m, 1H, OH, exchangeable), 6.21 (bs, 2H, NH_2, exchangeable), 7.11–7.17 (m, 1H, arom. H), 7.23–7.49 (m, 7H, arom. H),

7.69–7.77 (m, 1H, arom. H), 8.09 (bs, 1H, NHPh, exchangeable). ^{13}C NMR (101 MHz, DMSO-d_6) δ 164.03, 149.69, 149.47, 142.88, 142.35, 129.87, 128.31, 127.58, 126.46, 126.01, 125.50, 123.30, 120.26, 115.83, 112.66, 82.40, 71.29, 59.15, 53.79, 14.75. Anal calcd for $C_{21}H_{21}F_3N_4O_3$: C: 58.06; H: 4.87; N: 12.90. Found: C: 58.32; H: 4.83; N: 12.78.

4.1.2.11. Ethyl 5-amino-3-((3-chlorophenyl)amino)-1-(2-hydroxy-2-phenylethyl)-1H-pyrazole-4-carboxylate 3c. Yield: 37 %. White solid. Mp 110–113 °C (Et_2O/Ligroin). ^{1}H NMR (400 MHz, DMSO-d_6) δ 1.30 (t, J = 7.0 Hz, 3H, CH_3), 3.89–3.98 (m, 2H, NCH_2), 4.02–4.12 (m, 1H, CHOH), 4.24 (q, J = 7.0 Hz, 2H, CH_2O), 4.98–5.04 (m, 1H, CHPh), 5.65–5.71 (m, 1H, OH, exchangeable), 6.18 (bs, 2H, NH_2, exchangeable), 6.81–6.89 (m, 1H, arom. H), 7.19–7.45 (m, 7H, arom. H), 7.74–7.79 (m, 1H, arom. H), 8.16 (bs, 1H, NHPh, exchangeable). ^{13}C NMR (101 MHz, DMSO-d_6) δ 163.84, 149.45, 142.84, 133.25, 130.22, 128.26, 128.09, 127.55, 127.37, 126.29, 119.07, 115.68, 115.04, 82.13, 71.04, 58.93, 53.54, 14.54. Anal calcd for $C_{20}H_{21}ClN_4O_3$: C: 59.93; H: 5.28; N: 13.98. Found: C: 60.16; H: 5.25; N: 13.98.

4.1.2.12. 5-Amino-1-(2-hydroxy-2-phenylethyl)-3-((4-methoxyphenyl) amino)-1H-pyrazole-4-carboxylate 3d. Yield: 42 %. Yellow oil. ^{1}H NMR (400 MHz, DMSO-d_6) δ 1.30 (t, J = 7.0 Hz, 3H, CH_3), 3.85–3.94 (m, 2H, NCH_2), 3.97–4.10 (m, 1H, CHOH), 4.24 (q, J = 7.0 Hz, 2H, CH_2O), 4.96–5.05 (m, 1H, CHPh), 5.64–5.69 (m, 1H, OH, exchangeable), 6.11 (bs, 2H, NH_2, exchangeable), 6.81–6.87 (m, 2H, arom. H), 7.25–7.49 (m, 7H, arom. H), 7.83 (bs, 1H, NHPh, exchangeable). ^{13}C NMR (101 MHz, DMSO-d_6): δ 164.05, 153.00, 150.25, 149.55, 142.66, 135.06, 128.16, 126.31, 117.56, 115.68, 114.12, 71.08, 58.88, 55.38, 53.58, 14.64. Anal calcd for $C_{21}H_{24}N_4O_4$: C: 63.62; H: 6.10; N: 14.13. Found: C: 63.86; H: 5.96; N: 13.94.

4.1.2.13. Ethyl 5-amino-3-((3,4-dichlorophenyl)amino)-1-(2-hydroxy-2-phenylethyl)-1H-pyrazole-4-carboxylate 3e. Yield: 21 %. White solid. Mp 75–77 °C (EtOH). ^{1}H NMR (400 MHz, DMSO-d_6) δ 1.29 (t, J = 7.1 Hz, 3H, CH_3), 3.89–3.98 (m, 2H, NCH_2), 4.04–4.12 (m, 1H, CHOH), 4.24 (q, J = 7.1 Hz, 2H, CH_2O), 4.97–5.04 (m, 1H, CHPh), 5.66–5.70 (m, 1H, OH, exchangeable), 6.19 (bs, 2H, NH_2, exchangeable), 7.23–7.48 (m, 3H, arom. H), 7.89–8.02 (m, 5H, arom. H), 8.21 (bs, 1H, NHPh, exchangeable). ^{13}C NMR (101 MHz, DMSO-d_6) δ 163.95, 149.72, 149.14, 142.82, 141.74, 131.11, 130.49, 128.30, 127.58, 126.50, 120.66, 117.69, 117.03, 82.47, 71.23, 59.17, 53.77, 14.75. Anal calcd for $C_{20}H_{20}Cl_2N_4O_3$: C: 55.18; H: 4.63; N: 12.87. Found: C: 55.01; N: 12.65; H: 4.77.

4.1.2.14. Ethyl 5-amino-1-(2-hydroxy-2-phenylethyl)-3-(naphthalen-1-ylamino)-1H-pyrazole-4-carboxylate 3f. Yield: 35 %. White solid. Mp 165–166 °C (EtOH). ^{1}H NMR (400 MHz, DMSO-d_6) δ 1.36 (t, J = 7.1 Hz, 3H, CH_3), 3.93–4.03 (m, 2H, NCH_2), 4.06–4.16 (m, 1H, CHOH), 4.33 (q, J = 7.1 Hz, 2H, CH_2O), 5.02–5.11 (m, 1H, CHPh), 5.68–5.73 (m, 1H, OH, exchangeable), 6.22 (bs, 2H, NH_2, exchangeable), 7.23–7.66 (m, 9H, arom. H), 7.88–8.00 (m, 2H, arom. H), 8.26–8.35 (m, 1H, arom. H), 9.12 (bs, 1H, NHPh, exchangeable). ^{13}C NMR (101 MHz, DMSO-d_6) δ 164.61, 150.06, 149.29, 142.71, 136.02, 133.72, 128.77, 128.09, 127.36, 126.55, 126.37, 125.83, 125.74, 122.90, 119.46, 119.37, 110.95, 82.30, 71.11, 59.20, 53.65, 14.63. Calcd for $C_{24}H_{24}N_4O_3$: C: 69.21; H: 5.81; N: 13.45. Found: C: 69.13; H: 5.69; N: 13.55.

4.2. Biological evaluation

4.2.1. Anti-proliferative activity

MTT assays were performed using SKOV-3 (ovarian adenocarcinoma, ATCC, Manassas, VA); MCF-7 (breast adenocarcinoma, Biologic Bank and Cell Factory, IRCCS Policlinico San Martino, Genoa, Italy); Hep-G2 (hepatocellular carcinoma, ATCC, Manassas, VA); SK-MEL28 (skin melanoma, Biologic Bank and Cell Factory, IRCCS Policlinico San Martino, Genoa, Italy), GM-6114 (embryonic human fibroblast, ATCC, Manassas, VA); MDA-MB231 (breast adenocarcinoma, Biologic Bank and Cell Factory, IRCCS Policlinico San Martino, Genoa, Italy); HeLa (cervical adenocarcinoma, Biologic Bank and Cell Factory, IRCCS Policlinico San Martino, Genoa, Italy); SK-BR3 (breast andenocarcinoma, Biologic Bank and Cell Factory, IRCCS Policlinico San Martino, Genoa, Italy); A549 (lung carcinoma, Biologic Bank and Cell Factory, IRCCS Policlinico San Martino, Genoa, Italy); HUVEC (Human Umbilical Vein Endothelial Cells, ATCC, Manassas, VA) cell lines. All cell lines were grown in DMEM (with 10 % FBS, 2 mM Glutamine and 1 % pen-strep. All reagents were purchased from EuroClone (Milan, Italy) and incubated at 37 °C in 5 % CO_2 in a humidified environment. Briefly, all cell lines were plated in 96 well plates at a proper cell density to achieve about 80%–90 % of confluence at the end of the assay; 16 h after cell plating, the compounds were dissolved in DMSO to afford a 10 mM stock solution, diluted in growth medium and added at a final working concentration of 10 μM. After 48 h of incubation, 30 μL of MTT (3-(4,5-dimethyl-2-thiazolyl)-2,5-diphenyl-2H-tetrazolium bromide) diluted at 2 mg/mL with 1xPBS were added in each well. Then, after 4 h of incubation, the supernatant was removed and 100 μL/well of DMSO were used to dissolve the Formazan precipitate that can be found in vital cells. After 20 min, the optical density (OD) was measured at 570 nm using a plate reader. The results are expressed as a percentage of the control samples (100 %) in which the cell lines were incubated with the same amount of solvent but without any compounds. The assay was repeated three times. In each set, every single compound was tested six times. Means and standard deviations were calculated.

4.2.2. Endothelial tube formation assays

A 24-well plate was coated with matrigel (Becton Dickinson Labware, Franklin Lakes, NJ, USA) mixed to EGM-2 1:1 on ice and incubated at 37 °C for 30 min to allow gelation to occur. HUVEC cells were added to the top of the gelated matrigel at a density of 2 × 104 cells/well in the presence or absence of the treatments indicated for each experimental point. After 12 h, the images were captured using the EVOS optical microscope (10 ×) (Life technologies Corporation; Carlsbad, CA, USA). Tube formation was quantified by measuring the long axis of each tube and the number of branching points in 10 random fields per well at low power (10 ×) magnification through the ImageJ software (NIH, Bethesda, MD, USA) (“Angiogenesis Analyzer for ImageJ”). The mean tube length was determined for each well. The same procedure was carried out in presence of human PC MIA PaCa-2 cells (ATCC, Manassas, VA) supernatants. These cells were cultured in DMEM (with 10 % FBS, 2 mM Glutamine and 1 % pen-strep) (EuroClone; Milan, Italy) and incubated at 37 °C in 5 % CO_2 in a humidified environment. They were seeded at 1 × 10^6 in a p100 disk, after 24 h the growth medium was replaced by a medium free of FBS (serum starved –SS– medium) (MIA PaCa-2 sup) in order to induce a stress factor able to accelerate the release of soluble molecules from cells. After 72 h, SS supernatant was harvested, clarified and added on HUVEC cells in a ratio 1:1 with their basal growth medium in presence or not of **GeGe-3**, **2a** and **2d** (10 μM) compounds. After 12 h, the images were captured, and tube formation was quantified as described above.

4.2.3. In vitro wound-healing and invasion assays

In a 24-well plastic plate, HUVEC cells were seeded (density of 2 × 105, per well). After 24 h at 100 % confluency a wound was made in the cellular monolayer by gently scraping the cells with a sterile plastic p10 pipette tip. All experimental points were further treated with mitomycin C (10 μg/ml, Sigma-Aldrich; Saint Louis, MO, USA) to ensure the block of mitosis. The assay and the following analysis were performed as previously reported [32]. The wounded cells were photographed at time 0 and 24 h by using Axiovert 5 microscope with Axiocam 208 color (Carl Zeiss; Oberkochen, Germany). A 4 × phase contrast objective was used. The migration rate was determined by measuring the difference of the

distances covered of each wound edge from the initial time to the selected time-points. Cell invasiveness was studied using the *trans*-well cell culture (12 mm diameter, 8.0 pore size; Corning Incorporated, New York, NJ, USA), as previously described [27]. Briefly, the chambers, coated with matrigel (Becton Dickinson Labware; Franklin Lakes, NJ, USA) in a dilution 1:3 of serum-free medium, were stored at 37 °C until its gelation. Cells were plated in 350 μL of serum-free medium (2×10^4/insert) in the upper chamber of the *trans*-well. In the lower chamber a volume of 1.4 ml of growth medium was put with the treatments. Then the *trans*-wells were left for 24 h at 37 °C in 5 % CO_2-95 % air humidified atmosphere. After that, the medium was aspirated, the filters were washed twice with PBS 1 × and fixed with p-formaldehyde (4 % v/v in PBS; Lonza, Basel, Switzerland) for 10 min, then with 100 % methanol (Sigma-Aldrich; Saint Louis, MO, USA) for 20 min. The filters so fixed were stained with 0.5 % crystal violet prepared from stock crystal violet (powder, Merck Chemicals; Darmstadt, Germany) by distilled water and 20 % methanol (Sigma-Aldrich; Saint Louis, MO, USA) for 15 min. Then, the filters were washed again in PBS 1 × and cleaned with a cotton bud. The cells migrated to the lower surface were counted in ten random fields using EVOS optical microscope (10 ×) (Life technologies Corporation; Carlsbad, CA, USA).

4.2.4. Measurement of intracellular Ca^{2+} signaling

Intracellular Ca^{2+} concentrations [Ca^{2+}] were measured using the fluorescent Fluo-4 a.m. probe (Molecular Probes, Thermo Fisher Scientific, Waltham, MA, USA), as previously described [33–35]. Briefly, HUVEC cells were trypsinized, washed and placed in 1.5 mL tubes at 5 × 105/ml and then incubated with **GeGe-3** and with the compounds **2a** and **2d** 10 μM in PBS 1x for 1 h at room temperature. Then, cells were washed by centrifugation (5 min at 300 g) and incubated with 2.5 μM of Fluo-4 a.m. in 3 % DMSO (DMSO final concentration in each assay was 0.06 %) at 37 °C for 45 min in PBS 1x. Finally, cells were re-washed and the fluorescence in each sample was analyzed by a BD FACSCalibur cytometer using the 530/30 filter. Rapid kinetic measurement of fluorescence was performed by flow cytometry using Ca^{2+}-ionophore (ionomycin 1 mM; Sigma-Aldrich, St. Louis, MO, USA) and the chelating agent EDTA (5 mM, 15 min before; Sigma-Aldrich, St. Louis, MO, USA) as the positive and negative controls, respectively.

4.2.5. Confocal microscopy

HUVEC cells, untreated or treated with **GeGe-3** and compounds **2a** and **2d** (10 μM final concentration), were fixed on cover slips in p-formaldehyde (4 % vol/vol in PBS; Lonza; Basilea, Switzerland), permeabilized with Triton X-100 (0.2 % vol/vol in PBS; Lonza; Basilea, Switzerland), blocked with goat serum (20 % vol/vol in PBS; Lonza; Basilea, Switzerland) and then incubated with FITC-conjugated anti-F-actin (5 μg/ml; Phalloidin-FITC, Sigma-Aldrich, St. Louis, MO, USA) for 2 h at room temperature in the dark. To detect nuclei, Hoechst 33342 nucleic acid stain (1:5000 vol/vol; Molecular Probes, Thermo Fisher Scientific, Waltham, MA, USA) was used. Confocal analysis was performed with Zeiss ZEN Confocal Software (Carl Zeiss MicroImaging GmbH, Jena, Germany) as previously reported [32].

4.2.6. Docking simulations

The molecular structures of (R)-**2a** and (S)-**2a** were built by MOE2009.10 (builder module) and parameterized by MMFF94x force field. The docking poses within CALR were calculated by Autodock 4.2 [36]. After the removal of water molecules from the crystal structure of calreticulin (PDB code 3POW [37]) polar hydrogen and Gasteiger-Huckel charges were added. The missing residues in the pdb file (i.e., 10–15, 205–301 and 368) were not processed. The ligands root was defined automatically. A 60 × 60 × 60 Å grid (grid spacing 0.375 Å) was centered in the binding site of tetra saccharide binding site, as defined in the pdb file 3O0W [38] and electrostatic and affinity maps for each atom type of the ligand were calculated. The docking search was performed over 100 conformers using the Genetic Algorithm Local Search protocol as implemented in Autodock (population size: 50; rate of gene mutation: 0.02; rate of crossover: 0.8). The docking poses were clustered (rmsd: 2.0 Å) and the best conformation of the low energy highest populated cluster was selected as the binding conformation. Models analysis was carried out using the CCP4 program suite [39] The calculations were run on a Linux PC (Intel® processor Core™ i7-2600 CPU@3.40 GHz).

Fundings

This research was funded by Università degli Studi di Genova, grant Fondi di Ricerca di Ateneo (FRA). E.I. and M.P. acknowledge the support of the Italian Ministry of Health (Ricerca Corrente).

CRediT authorship contribution statement

Matteo Lusardi: Writing – original draft, Methodology, Investigation. **Raffaella Belvedere:** Writing – review & editing, Methodology, Investigation. **Antonello Petrella:** Writing – review & editing, Investigation, Conceptualization. **Erika Iervasi:** Writing – review & editing, Investigation, Data curation. **Marco Ponassi:** Writing – review & editing, Methodology, Investigation, Funding acquisition. **Chiara Brullo:** Writing – review & editing, Methodology, Funding acquisition, Conceptualization. **Andrea Spallarossa:** Writing – review & editing, Investigation, Funding acquisition, Conceptualization.

Declaration of competing interest

The authors declare that they have no known competing financial interests or personal relationships that could have appeared to influence the work reported in this paper.

Data availability

Data will be made available on request.

Acknowledgements

The authors thank Dr. M. Anzaldi, F. Rapetti and R. Raggio for spectral recording and elemental analysis.

Appendix A. Supplementary data

Supplementary data to this article can be found online at https://doi.org/10.1016/j.ejmech.2024.116715.

References

[1] A.C. Dudley, A.W. Griffioen, The modes of angiogenesis: an updated perspective, Angiogenesis 26 (2023) 477–480, https://doi.org/10.1007/s10456-023-09895-4.
[2] D. La Mendola, M.L. Trincavelli, C. Martini, Angiogenesis in disease, Int. J. Mol. Sci. 23 (2022) 10962, https://doi.org/10.3390/ijms231810962.
[3] A. Mukwaya, L. Jensen, N. Lagali, Relapse of pathological angiogenesis: functional role of the basement membrane and potential treatment strategies, Exp. Mol. Med. 53 (2021) 189–201, https://doi.org/10.1038/s12276-021-00566-2.
[4] M. Rajabi, S. Mousa, The role of angiogenesis in cancer treatment, Biomedicines 5 (2017) 34, https://doi.org/10.3390/biomedicines5020034.
[5] J.-H. Jeong, U. Ojha, Y.M. Lee, Pathological angiogenesis and inflammation in tissues, Arch Pharm. Res. (Seoul) 44 (2021) 1–15, https://doi.org/10.1007/s12272-020-01287-2.
[6] J. Stebbing, L.C. Lit, H. Zhang, R.S. Darrington, O. Melaiu, B. Rudraraju, G. Giamas, The regulatory roles of phosphatases in cancer, Oncogene 33 (2014) 939–953, https://doi.org/10.1038/onc.2013.80.
[7] J.-J. Ventura, Á.R. Nebreda, Protein kinases and phosphatases as therapeutic targets in cancer, Clin. Transl. Oncol. 8 (2006) 153–160, https://doi.org/10.1007/s12094-006-0005-0.
[8] L. Munaron, C. Tomatis, A.F. Pla, The secret marriage between calcium and tumor angiogenesis, Technol. Cancer Res. Treat. 7 (2008) 335–339, https://doi.org/10.1177/153303460800700408.
[9] R. Zini, P. Guglielmelli, D. Pietra, E. Rumi, C. Rossi, S. Rontauroli, E. Genovese, T. Fanelli, L. Calabresi, E. Bianchi, S. Salati, M. Cazzola, E. Tagliafico, A.

M. Vannucchi, R. Manfredini, On behalf of the AGIMM (AIRC Gruppo Italiano Malattie Mieloproliferative) investigators, CALR mutational status identifies different disease subtypes of essential thrombocythemia showing distinct expression profiles, Blood Cancer J. 7 (2017) 638, https://doi.org/10.1038/s41408-017-0010-2.

[10] Y. Liu, W. Wei, C. Hong, Y. Wang, X. Sun, J. Ma, F. Zheng, Calreticulin induced endothelial ICAM-1 up-regulation associated with tristetraprolin expression alteration through PI3K/Akt/eNOS/p38 MAPK signaling pathway in rheumatoid arthritis, Mol. Immunol. 107 (2019) 10–20, https://doi.org/10.1016/j.molimm.2019.01.005.

[11] Y. Jiao, H. Ding, S. Huang, Y. Liu, X. Sun, W. Wei, J. Ma, F. Zheng, Bcl-XL and Mcl-1 upregulation by calreticulin promotes apoptosis resistance of fibroblast-like synoviocytes via activation of PI3K/Akt and STAT3 pathways in rheumatoid arthritis, Clin. Exp. Rheumatol. 36 (2018) 841–849.

[12] O. Bruno, C. Brullo, F. Bondavalli, S. Schenone, A. Ranise, N. Arduino, M. B. Bertolotto, F. Montecucco, L. Ottonello, F. Dallegri, M. Tognolini, V. Ballabeni, S. Bertoni, E. Barocelli, Synthesis and biological evaluation of *N* -pyrazolyl- *N* '-alkyl/benzyl/phenylureas: a new class of potent inhibitors of interleukin 8-induced neutrophil chemotaxis, J. Med. Chem. 50 (2007) 3618–3626, https://doi.org/10.1021/jm0704402.

[13] E. Meta, C. Brullo, A. Sidibe, B.A. Imhof, O. Bruno, Design, synthesis and biological evaluation of new pyrazolyl-ureas and imidazopyrazolecarboxamides able to interfere with MAPK and PI3K upstream signaling involved in the angiogenesis, Eur. J. Med. Chem. 133 (2017) 24–35, https://doi.org/10.1016/j.ejmech.2017.03.066.

[14] B. Marengo, E. Meta, C. Brullo, C. De Ciucis, R. Colla, A. Speciale, O. Garbarino, O. Bruno, C. Domenicotti, Biological evaluation of pyrazolyl-urea and dihydro-imidazo-pyrazolyl-urea derivatives as potential anti-angiogenetic agents in the treatment of neuroblastoma, Oncotarget 11 (2020) 3459–3472, https://doi.org/10.18632/oncotarget.27733.

[15] E. Morretta, A. Sidibè, A. Spallarossa, A. Petrella, E. Meta, O. Bruno, M.C. Monti, C. Brullo, Synthesis, functional proteomics and biological evaluation of new 5-pyrazolyl ureas as potential anti-angiogenic compounds, Eur. J. Med. Chem. 226 (2021) 113872, https://doi.org/10.1016/j.ejmech.2021.113872.

[16] R. Belvedere, E. Morretta, N. Novizio, S. Morello, O. Bruno, C. Brullo, A. Petrella, The pyrazolyl-urea Gege3 inhibits the activity of ANXA1 in the angiogenesis induced by the pancreatic cancer derived EVs, Biomolecules 11 (2021) 1758, https://doi.org/10.3390/biom11121758.

[17] E. Meta, B.A. Imhof, P. Ropraz, R.J. Fish, C. Brullo, O. Bruno, A. Sidibé, The pyrazolyl-urea GeGe3 inhibits tumor angiogenesis and reveals dystrophia myotonica protein kinase (DMPK)1 as a novel angiogenesis target, Oncotarget (2017) 108195–108212, https://doi.org/10.18632/oncotarget.22598.

[18] E. Morretta, R. Belvedere, A. Petrella, A. Spallarossa, F. Rapetti, O. Bruno, C. Brullo, M.C. Monti, Novel insights on the molecular mechanism of action of the anti-angiogenic pyrazolyl-urea GeGe-3 by functional proteomics, Bioorg. Chem. 115 (2021) 105168, https://doi.org/10.1016/j.bioorg.2021.105168.

[19] M. Lusardi, B. Wehrle-Haller, A. Sidibe, M. Ponassi, E. Iervasi, C. Rosano, C. Brullo, A. Spallarossa, Novel 5-aminopyrazoles endowed with anti-angiogenetic properties: Design, synthesis and biological evaluation, Eur. J. Med. Chem. 260 (2023) 115727, https://doi.org/10.1016/j.ejmech.2023.115727.

[20] M. Lusardi, A. Profumo, C. Rotolo, E. Iervasi, C. Rosano, A. Spallarossa, M. Ponassi, Regioselective synthesis, structural Characterization, and antiproliferative activity of novel tetra-substituted Phenylaminopyrazole derivatives, Molecules 27 (2022) 5814, https://doi.org/10.3390/molecules27185814.

[21] M. Lusardi, C. Rotolo, M. Ponassi, E. Iervasi, C. Rosano, A. Spallarossa, One-pot synthesis and antiproliferative activity of highly functionalized pyrazole derivatives, ChemMedChem 17 (2022) e202100670, https://doi.org/10.1002/cmdc.202100670.

[22] M.G. Tonnesen, X. Feng, R.A.F. Clark, Angiogenesis in wound healing, J. Invest. Dermatol. Symp. Proc. 5 (2000) 40–46, https://doi.org/10.1046/j.1087-0024.2000.00014.x.

[23] A.J. Singer, R.A.F. Clark, Cutaneous wound healing, N. Engl. J. Med. 341 (1999) 738–746, https://doi.org/10.1056/NEJM199909023411006.

[24] R.A.F. Clark, P. DellaPelle, E. Manseau, J.M. Lanigan, H.F. Dvorak, R.B. Colvin, Blood vessel Fibronectin Increases in Conjunction with endothelial cell proliferation and capillary Ingrowth during wound healing, J. Invest. Dermatol. 79 (1982) 269–276, https://doi.org/10.1111/1523-1747.ep12500076.

[25] P. Carmeliet, R.K. Jain, Molecular mechanisms and clinical applications of angiogenesis, Nature 473 (2011) 298–307, https://doi.org/10.1038/nature10144.

[26] X. Jiang, J. Wang, X. Deng, F. Xiong, S. Zhang, Z. Gong, X. Li, K. Cao, H. Deng, Y. He, Q. Liao, B. Xiang, M. Zhou, C. Guo, Z. Zeng, G. Li, X. Li, W. Xiong, The role of microenvironment in tumor angiogenesis, J. Exp. Clin. Cancer Res. 39 (2020) 204, https://doi.org/10.1186/s13046-020-01709-5.

[27] R. Belvedere, V. Bizzarro, A. Popolo, F. Dal Piaz, M. Vasaturo, P. Picardi, L. Parente, A. Petrella, Role of intracellular and extracellular annexin A1 in migration and invasion of human pancreatic carcinoma cells, BMC Cancer 14 (2014) 961, https://doi.org/10.1186/1471-2407-14-961.

[28] M. Michalak, J. Groenendyk, E. Szabo, L.I. Gold, M. Opas, Calreticulin, a multi-process calcium-buffering chaperone of the endoplasmic reticulum, Biochem. J. 417 (2009) 651–666, https://doi.org/10.1042/BJ20081847.

[29] V. Bizzarro, R. Belvedere, F. Dal Piaz, L. Parente, A. Petrella, Annexin A1 induces skeletal muscle cell migration acting through formyl peptide receptors, PLoS One (2012) e48246, https://doi.org/10.1371/journal.pone.0048246.

[30] G.H. Elgemeie, A.H. Elghandour, G.W.A. Elaziz, Novel Cyanoketene *N* , *S* -acetals and pyrazole derivatives using Potassium 2-Cyanoethylene-1-thiolates, Synth. Commun. 37 (2007) 2827–2834, https://doi.org/10.1080/00397910701473317.

[31] C.J. Shishoo, M.B. Devani, V.S. Bhadti, S. Ananthan, G.V. Ullas, Heterocyclization of functionalized ketene acetals: synthesis of pyrimidines vinylamidine intermediates, Tetrahedron Lett. 25 (1984) 1291–1292, https://doi.org/10.1016/S0040-4039(01)80137-4.

[32] R. Belvedere, N. Novizio, M. Palazzo, E. Pessolano, A. Petrella, The pro-healing effects of heparan sulfate and growth factors are enhanced by the heparinase enzyme: new association for skin wound healing treatment, Eur. J. Pharmacol. 960 (2023) 176138, https://doi.org/10.1016/j.ejphar.2023.176138.

[33] R. Belvedere, N. Novizio, E. Pessolano, A. Tosco, D. Eletto, A. Porta, P. Campiglia, M. Perretti, A. Filippelli, A. Petrella, Heparan sulfate binds the extracellular Annexin A1 and blocks its effects on pancreatic cancer cells, Biochem. Pharmacol. 182 (2020) 114252, https://doi.org/10.1016/j.bcp.2020.114252.

[34] V. Bizzarro, R. Belvedere, E. Pessolano, L. Parente, F. Petrella, M. Perretti, A. Petrella, Mesoglycan induces keratinocyte activation by triggering syndecan-4 pathway and the formation of the annexin A1/S100A11 complex, J. Cell. Physiol. 234 (2019) 20174–20192, https://doi.org/10.1002/jcp.28618.

[35] A.M. Rossi, C.W. Taylor, Reliable measurement of free Ca2+ concentrations in the ER lumen using Mag-Fluo-4, Cell Calcium 87 (2020) 102188, https://doi.org/10.1016/j.ceca.2020.102188.

[36] G.M. Morris, R. Huey, W. Lindstrom, M.F. Sanner, R.K. Belew, D.S. Goodsell, A. J. Olson, AutoDock4 and AutoDockTools4: automated docking with selective receptor flexibility, J. Comput. Chem. 30 (2009) 2785–2791, https://doi.org/10.1002/jcc.21256.

[37] A. Chouquet, H. Païdassi, W.L. Ling, P. Frachet, G. Houen, G.J. Arlaud, C. Gaboriaud, X-ray structure of the human calreticulin alobular domain reveals a peptide-binding area and suggests a multi-molecular mechanism, PLoS One 6 (2011) e17886, https://doi.org/10.1371/journal.pone.0017886.

[38] G. Kozlov, C.L. Pocanschi, A. Rosenauer, S. Bastos-Aristizabal, A. Gorelik, D. B. Williams, K. Gehring, Structural basis of carbohydrate recognition by calreticulin, J. Biol. Chem. 285 (2010) 38612–38620, https://doi.org/10.1074/jbc.M110.168294.

[39] M.D. Winn, C.C. Ballard, K.D. Cowtan, E.J. Dodson, P. Emsley, P.R. Evans, R. M. Keegan, E.B. Krissinel, A.G.W. Leslie, A. McCoy, S.J. McNicholas, G. N. Murshudov, N.S. Pannu, E.A. Potterton, H.R. Powell, R.J. Read, A. Vagin, K. S. Wilson, Overview of the *CCP* 4 suite and current developments, Acta Crystallographica D Biology Crystallography 67 (2011) 235–242, https://doi.org/10.1107/S0907444910045749.